The Astrophysical Journal, 905:142 (12pp), 2020 December 20 https://doi.org/10.3847/1538-4357/abc480

Coherent Events at Ion Scales in the Inner Heliosphere: Parker Solar Probe Observations during the First Encounter

Denise Perrone[1], Roberto Bruno[2], Raffaella D'Amicis[2], Daniele Telloni[3], Rossana De Marco[2], Marco Stangalini[1], Silvia Perri[4], Oreste Pezzi[5,6,7], Olga Alexandrova[8], and Stuart D. Bale[9,10,11,12]
[1] ASI—Italian Space Agency, via del Politecnico snc, I-00133 Rome, Italy; denise.perrone@asi.it
[2] National Institute for Astrophysics, Institute for Space Astrophysics and Planetology, Via del Fosso del Cavaliere 100, I-00133 Roma, Italy
[3] National Institute for Astrophysics, Astrophysical Observatory of Torino, Via Osservatorio 20, I-10025 Pino Torinese, Italy
[4] Dipartimento di Fisica, Università della Calabria, Rende, Italy
[5] Gran Sasso Science Institute, Viale F. Crispi 7, I-67100 L'Aquila, Italy
[6] INFN/Laboratori Nazionali del Gran Sasso, Via G. Acitelli 22, I-67100 Assergi (AQ), Italy
[7] Istituto per la Scienza e Tecnologia dei Plasmi, CNR, Via Amendola 122/D, I-70126 Bari, Italy
[8] LESIA, Observatoire de Paris, Université PSL, CNRS, Sorbonne Université, Univ. Paris Diderot, Sorbonne Paris Cité, 5 place Jules Janssen, F-92195 Meudon, France
[9] Space Sciences Laboratory, University of California, Berkeley, CA, USA
[10] Physics Department, University of California, Berkeley, CA, USA
[11] The Blackett Laboratory, Imperial College London, London, UK
[12] School of Physics and Astronomy, Queen Mary University of London, London, UK
Received 2020 October 2; revised 2020 October 22; accepted 2020 October 22; published 2020 December 22

Abstract

The Parker Solar Probe mission has shown the ubiquitous presence of strong magnetic field deflections, namely switchbacks, during its first perihelion where it was embedded in a highly Alfvénic slow stream. Here, we study the turbulent magnetic fluctuations around ion scales in three intervals characterized by a different switchback activity, identified by the behavior of the magnetic field radial component, B_r. *Quiet* (B_r does not show significant fluctuations), *weakly disturbed* (B_r has strong fluctuations but no reversals), and *highly disturbed* (B_r has full reversals) periods also show different behavior for ion quantities. However, the spectral analysis shows that each stream is characterized by the typical Kolmogorov/Kraichnan power law in the inertial range, followed by a break around the characteristic ion scales. This frequency range is characterized by strong intermittent activity, with the presence of noncompressive coherent events, such as current sheets, vortex-like structures, and wave packets identified as ion cyclotron modes. Although all these events have been detected in the three periods, they have different influences in each of them. Current sheets are dominant in the *highly disturbed* period, wave packets are the most common in the *quiet* interval; while, in the *weakly disturbed* period, a mixture of vortices and wave packets is observed. This work provides an insight into the heating problem in collisionless plasmas, fitting in the context of the new solar missions, and, especially for Solar Orbiter, which will allow an accurate magnetic connectivity analysis to link the presence of different intermittent events to the source region.

Unified Astronomy Thesaurus concepts: Space plasmas (1544); Interplanetary turbulence (830); Solar wind (1534)

1. Introduction

A puzzling aspect of the fast solar-wind dynamics consists of the empirical evidence that it is hotter than expected for an adiabatic expanding gas (Marsch et al. 1982; Lopez & Freeman 1986; Freeman 1988; Williams et al. 1995; Hellinger et al. 2013; Borovsky & Gary 2014; Perrone et al. 2019a, 2019b). Understanding the physical mechanisms of dissipation, and the related heating, in such a turbulent collision-free system, represents nowadays one of the key issues of plasma physics. Moreover, explaining how irreversible heating is accomplished represents a key challenge for thermodynamics in general, since any mechanism in which collisions are not present is lacking the part of the heating process related to the irreversible degradation of information (Pezzi et al. 2019; Matthaeus et al. 2020).

Spacecraft measurements generally reveal that the solar-wind plasma is in a state of fully developed turbulence (Coleman 1968; Bruno & Carbone 2013). The energy injected by the Sun into the Heliosphere, in the form of large-wavelength fluctuations, e.g., Alfvén waves, is channeled toward short scales through a turbulent cascade until it can be eventually transferred to the plasma particles as heat (Alexandrova et al. 2009; Kiyani et al. 2009; Sahraoui et al. 2010). The magnetic power spectrum manifests at scales corresponding to the inertial range a behavior reminiscent of the power law that characterizes fluid turbulence (Kolmogorov 1941; Tu & Marsch 1995). Then, the turbulent cascade extends to smaller scales down to a wavelength range where ions become unmagnetized and the plasma dynamics is governed by particle kinetic properties. At these scales, around ion characteristic lengths, different physical processes come into play, leading to both changes in the spectral shape (Leamon et al. 1998; Bale et al. 2005; Alexandrova et al. 2013; Lion et al. 2016) and departure of the ion distribution functions from the thermodynamic equilibrium (Marsch 2006; Servidio et al. 2015; Sorriso-Valvo et al. 2019).

Turbulence in the solar wind is strongly space-localized and the degree of nonhomogeneity increases as the spatial scales decrease. This phenomenon is called intermittency. It is worth pointing out that this is generally true in the inertial range of the turbulent cascade. However, in the sub ion range, it has been observed that the degree of nonhomogeneity does not constantly increase toward smaller scales (Kiyani et al. 2013; Chen et al. 2014; Yordanova et al. 2015; Carbone et al. 2018).

Intermittency, recovered in both magnetic field and plasma parameters (Veltri & Mangeney 1999; Bruno et al. 2003; Salem et al. 2009; Bruno 2019), has been observed to evolve with distance from the Sun and it is due to the presence of coherent structures (Bruno et al. 2003; Greco et al. 2012a), which can be described as strong nonhomogeneities in the magnetic field (Retinò et al. 2007; Perri et al. 2012; Greco & Perri 2014; Perrone et al. 2016, 2017) over a wide range of scales (Greco et al. 2016; Lion et al. 2016). Near these coherent structures, particle energization, temperature anisotropy, and strong deviation from Maxwellian have been observed in both in situ data and numerical simulations (Matteini et al. 2010; Osman et al. 2011; Greco et al. 2012b; Servidio et al. 2012, 2015, 2017; Perrone et al. 2013, 2014; Wu et al. 2013; Pezzi et al. 2018; Sorriso-Valvo et al. 2018).

Recently, a statistical study of coherent structures at ion scales has been performed in both slow (Perrone et al. 2016) and fast (Perrone et al. 2017) solar wind at 1 au by using Cluster observations. It has been shown, for the first time, that different families of structures characterize the ion scales of the turbulent cascade of solar-wind plasma. This means that different mechanisms of dissipation occur at ion scales, since different structures interact with particles in different ways. Compressive structures, such as magnetic holes, solitons and shocks, and Alfvénic structures, in the form of current sheets and vortices, are observed in slow solar wind (Perrone et al. 2016). In fast solar wind, we found that the ion scales are dominated, in terms of time in the signal, by Alfvén vortices, with a small and/or finite compressive part. Current sheets are also observed but no compressive structures are found (Perrone et al. 2017).

Slow wind presents a more complex nature in terms of observed physical phenomena, both because it originates from equatorial regions on the Sun where the magnetic field configuration is dominated by complex closed field lines and because it is characterized by the presence of "fossil" coronal structures that propagate in the interplanetary medium (see, e.g., Borovsky 2008). Moreover, slow wind has higher collisionality than the fast wind (see, e.g., Salem et al. 2003; Kasper et al. 2008; D'Amicis et al. 2019) and of course a longer propagation time, which implies a longer time to evolve. Finally, the presence of a significant percentage of compressive structures at ion scales, that move in the flow (Perrone et al. 2016), may lead to the generation of additional instabilities, with effects on particles (Hellinger et al. 2019), with respect to the ion instabilities already present in the majority of solar wind streams (Klein et al. 2018). However, it is also true that, in fast wind, alpha particles have higher drift speeds with respect to the slow wind, and may generate further instabilities (Borovsky & Gary 2014). It is worth noting that, although linear instabilities are supported by the plasma (Klein et al. 2018), their significance in a strongly turbulent environment is still under debate (Matthaeus et al. 2014; Gary et al. 2020; Qudsi et al. 2020).

A large variety of magnetic structures have also been detected in the inner heliosphere by using Messenger magnetic field observations at 0.3 au (Greco & Perri 2014) during the minimum of solar cycle 23. Unfortunately, due to the unavailability of the plasma data on the spacecraft, no information about the stream in terms of origin and/or speed is possible. However, by looking at magnetic field fluctuations, both Alfvénic, such as rotational and tangential discontinuities, and compressive structures, namely shocks and magnetic holes, have been identified. The study of the presence of coherent structures in the inner heliosphere, especially in regions close to the Sun, could help to explore the dynamical development of solar wind turbulence. Thanks to the Parker Solar Probe (PSP) spacecraft (Fox et al. 2016), launched in August 2018, it is possible to study the presence and, eventually, the nature of coherent structures in a completely unexplored environment.

During its first perihelion, PSP revealed the presence of a large number of S-shaped magnetic structures that produce patches of large, intermittent magnetic field reversals, namely "switchbacks" (Bale et al. 2019; Dudok de Wit et al. 2020), heat flux reversals and isolated intermittent velocity enhancements, namely "spikes" (Kasper et al. 2019; Horbury et al. 2020). It is worth remarking that magnetic switchbacks have already been observed at different radial distances from the Sun by previous missions (Behannon & Burlaga 1981; Tsurutani et al. 1994; Kahler et al. 1996; Balogh et al. 1999; Landi et al. 2006; Borovsky 2016) but always in fast wind. Using PSP data, Krasnoselskikh et al. (2020) performed a detailed analysis on three selected structures, representative of three different groups of switchbacks, namely (i) Alfvénic-like structures, (ii) compressional-like structures, and (iii) full reversals of the radial component of the magnetic field vector. The size of these structures is large compared to the typical characteristic ion scales, except for their boundaries where flowing currents were found. Moreover, a rather intense wave activity, close to the edges of these structures has also been observed. This analysis suggests that these structures are localized twisted magnetic tubes moving with respect to the surrounding plasma.

In this paper, we study the nature of the turbulent magnetic fluctuations around ion scales in three PSP intervals with different characteristics during its first perihelion. In particular, by looking at the radial component of the magnetic field vector, B_r, we selected 1h15 intervals where (i) B_r is almost constant, (ii) B_r has strong fluctuations but no reversals, and (iii) B_r has full reversals. In these three intervals, we focus on intermittency and we statistically study the observed coherent events. Examples of these events are also shown below.

The paper is organized as follows: in Section 2 we present the main characteristics of the first PSP encounter and we select the three intervals for the analysis; in Section 3 we show the results of statistical studies and we present examples of different coherent events; and in Section 4 we summarize the results and discuss our conclusions.

2. First PSP Encounter

In 2018 November PSP completed its first perihelion passage at about 0.17 au from the Sun, sampling the solar wind far closer than before. During this first encounter, the spacecraft was almost corotating with the Sun and observed a long interval of slow, but Alfvénic, wind originating from a small equatorial coronal hole (Bale et al. 2019; Badman et al. 2020), characterized by the presence of isolated intermittent velocity enhancements (Kasper et al. 2019; Horbury et al. 2020) associated with magnetic field deflections (Bale et al. 2019; Dudok de Wit et al. 2020).

Although the standard classification of the solar wind on speed is widely accepted, it cannot always explain the observations. Alfvénic slow wind represents a statistically important solar wind regime that, apart from the speed, shares common characteristics with fast wind. It has extensively been

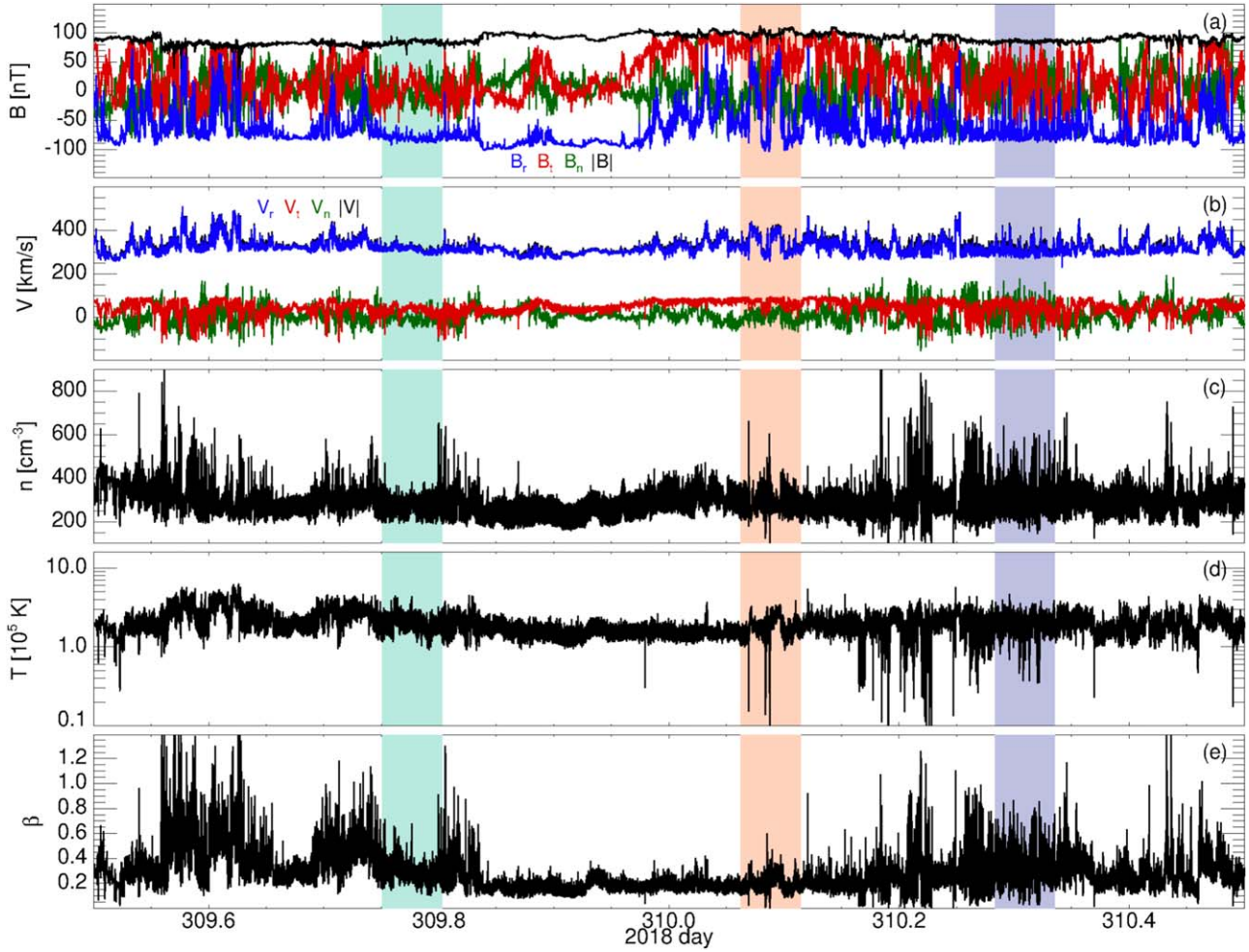

Figure 1. Overview of solar wind data during the first perihelion of PSP at ∼0.17 au. From top to bottom: three components in RTN (radial in blue, tangential in red, and normal in green) and magnitude (in black) of the magnetic (a) and velocity (b) field vectors, ion density (c), temperature (d), and plasma beta (e). The colored bands denote three different periods, lasting 1h15, of quiet (green), weakly disturbed (violet), and highly disturbed (orange) switchback activity.

studied both at 1 au (D'Amicis & Bruno 2015; D'Amicis et al. 2019) and in the inner heliosphere (Perrone et al. 2020; Stansby et al. 2020), suggesting a similar origin for both fast and Alfvénic slow wind, namely coronal holes. PSP observations support this interpretation.

In this paper, we consider a one-day period (from 12:00 UT on 2018 November 5) around perihelion (see Figure 1) to study the nature of the turbulent magnetic fluctuations in three 1h15 intervals, with different characteristics in terms of switchbacks. We mainly focus on magnetic field measurements from the fluxgate Magnetometer (MAG), which is part of the FIELDS suite (Bale et al. 2016). We use the full cadence observations of the three components of the magnetic field vector, having a sampling rate of 293 Hz. Moreover, in order to set a context of the environment, we consider the solar wind bulk plasma properties measured by the Solar Probe Cup (SPC; Case et al. 2020), a solar-facing Faraday cup, from the SWEAP instrument suite (Kasper et al. 2016). The ion density, n, and velocity, $\boldsymbol{V}$, are derived by taking moments of the one-dimensional ion velocity distribution obtained by the current spectra, the primary data product of the SPC sensor, with a cadence of about 0.87 s. The ion temperature, T, is also estimated from the ion thermal speed, v_{th}, which is also a regular derived product of SPC, as $T = mv_{th}^2/2k_B$, where m is the proton mass and k_B is the Boltzmann's constant.

2.1. Interval Characterization

In Figure 1, an overview of the solar wind in the considered 1 day period around the first perihelion of PSP is summarized, where magnetic field data have been downsampled to comply with the resolution of particle measurements. Panels (a) and (b) show the three components in the RTN reference frame (radial in blue, tangential in red, and normal in green) and magnitude (in black) of the magnetic and velocity field vectors, respectively. It is clear, especially looking at the radial component of the magnetic field vector, that different regimes lie in this 1 day interval, where the switchback activity significantly varies. In particular, we observe periods where B_r is almost constant and periods where B_r has strong fluctuations and sometimes fully reverses. Therefore, we decided to perform our studies on three 1h15 selected periods separately, denoted in Figure 1 by colored bands. From now on, we will refer to quiet (green band), weakly disturbed (violet band), and highly disturbed (orange band) periods if B_r does not show significant fluctuations, B_r has strong fluctuations but no reversals, and B_r has full reversals, respectively. Panels (c) and (d) display the ion density and temperature, respectively. Differences are also recovered in these quantities with respect to the three selected periods. In particular, the largest fluctuations around a mean value are found in the weakly disturbed interval, while in the

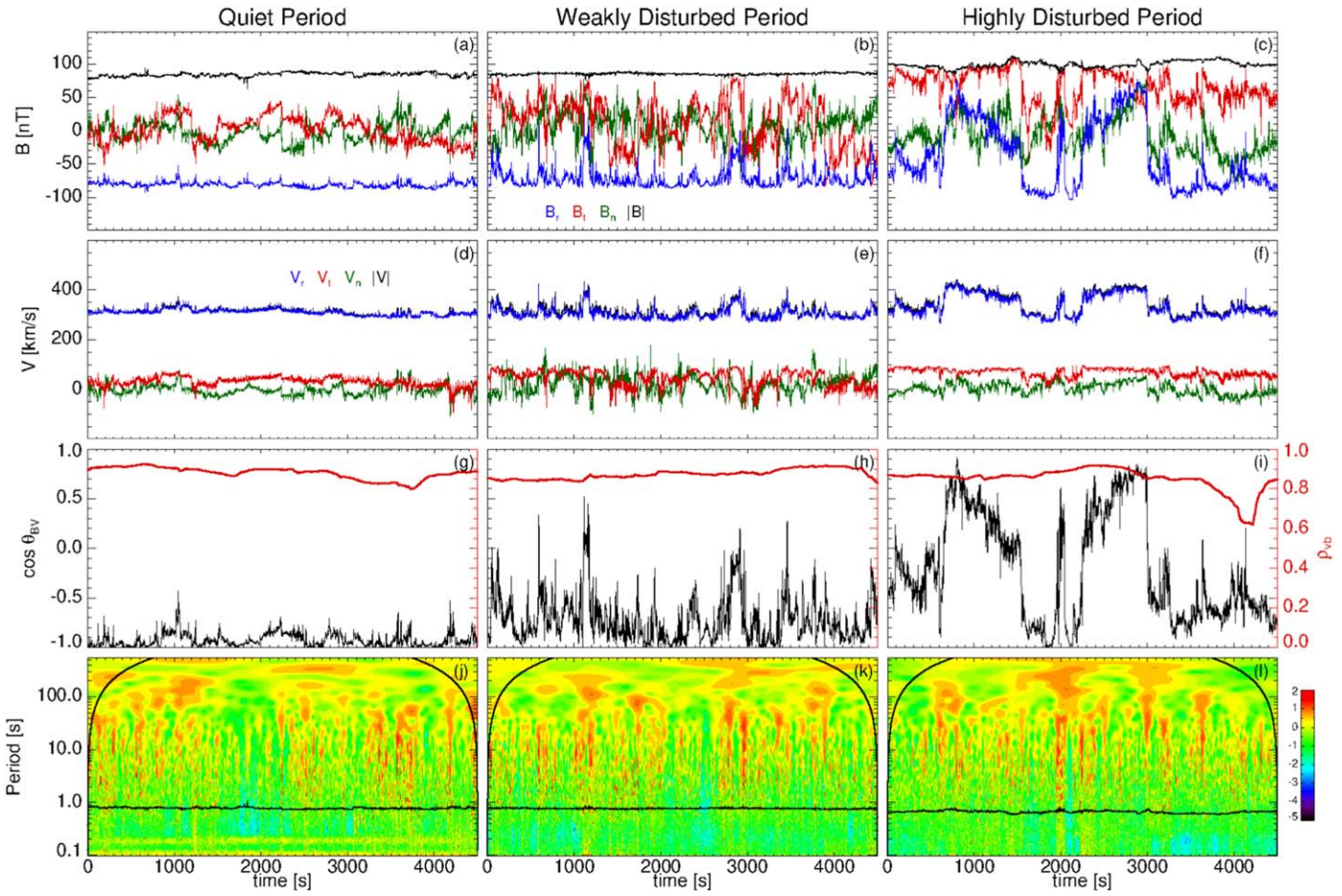

Figure 2. Characteristics of the quiet (left column), weakly disturbed (middle column), and highly disturbed (right column) periods. From top to bottom: zoom of Figure 1 in the selected intervals for the magnetic (first row) and velocity (second row) field vectors; cosine of the angle between the magnetic and velocity field vectors in black and the *v*–*b* correlation coefficient, ρ_{vb}, computed at 30 minute scales, in red (third row); zoom-in of timescales of the logarithmic contour plots of the local intermittency measure (LIM) of the total magnetic field fluctuations (fourth row). In the latter, black lines denote the ion cyclotron timescale and curved lines, at each side of the plots, indicate the cone of influence.

Table 1
Typical Solar Wind Parameters, Averaged within Each 1h15 Selected Period, Observed by PSP at 0.17 au

Period	Day	UT	B (nT)	V (km s^{-1})	n (cm^{-3})	T (10^5 K)
Quiet	309	18:14:24	84 ± 3	312 ± 13	301 ± 33	1.9 ± 0.4
Weakly disturbed	310	06:47:31	86 ± 2	311 ± 25	331 ± 52	2.0 ± 0.5
Highly disturbed	310	01:29:17	100 ± 5	345 ± 45	306 ± 42	1.8 ± 0.5
Period		β	V_A (km s^{-1})	λ_i (km)	ρ_i (km)	Ω_{ci} (rad s^{-1})
Quiet		0.32 ± 0.08	99 ± 5	13.2 ± 0.7	7.4 ± 0.7	8.1 ± 0.3
Weakly disturbed		0.33 ± 0.11	103 ± 9	12.6 ± 1.1	7.1 ± 0.9	8.2 ± 0.2
Highly disturbed		0.18 ± 0.05	126 ± 10	13.1 ± 1.0	5.5 ± 0.8	9.5 ± 0.5

Note. Day and UT information refers to the starting time. The errors refer to the standard deviation evaluated in each interval.

highly disturbed one a change in the behavior is observed in correspondence of the reversals. Finally, in panel (e), we show the ion plasma beta, β, defined as the ratio between ion kinetic and magnetic pressures. Also in this case, we found the same features observed for the density.

Looking at the typical solar-wind parameters (listed in Table 1), averaged within each selected interval considered in this study, we observe that quiet and weakly disturbed periods have almost the same values as the magnitude of the magnetic and velocity field vectors, while in the highly disturbed period higher values are found. Taking into account their standard deviation, we observe that larger amplitudes of the fluctuations are found, as expected, in the highly disturbed interval, namely $\Delta B/B \sim 0.05$ and $\Delta V/V \sim 0.13$. The same trend for the mean values is observed for the characteristic derived quantities, such as the Alfvén speed, V_A, and the ion cyclotron frequency, Ω_{ci}. Moreover, we see that the ion density is larger for the weakly disturbed period, probably due to the presence of stronger fluctuations, while the temperature and the ion skin depth, λ_i, have similar values in all the three intervals. Finally, for both

the ion plasma beta and Larmor radius, ρ_i, lower values are found in the highly disturbed period ($\beta \sim 0.18$ and $\rho_i \sim 5.5$ km, respectively), while higher and similar values are observed in both the weakly disturbed and quiet intervals ($\beta \sim 0.3$ and $\rho_i \sim 7$ km).

In Figure 2, we look at the three periods in more detail. The first two rows are just a zoom of Figure 1 in the selected intervals for the magnetic and velocity field vectors, respectively. Here, we can better appreciate the behavior of B_r: in the quiet (a) period it is almost constant, in the weakly disturbed (b) period it undergoes short scale variations, and in the highly disturbed (c) period it largely rotates. Moreover, quiet (a) and weakly disturbed (b) periods have almost constant magnetic field magnitude, while B in the highly disturbed period (c) is more variable. Furthermore, for the velocity field vector, we observed an increase of spikes in V_r for the weakly disturbed (e) and highly disturbed (f) intervals with respect to the quiet one (d). Finally, the V_r component is highly correlated with B_r in all three periods, which of course indicates a high level of Alfvénicity in the wind. To better stress this aspect, in the third row, we plot in black the cosine of the angle between $\boldsymbol{B}$ and $\boldsymbol{V}$ and in red a zoom-in of the three intervals of the v–b correlation coefficient, ρ_{vb}, computed over 30 minute running windows on the 1 day period shown in Figure 1. All three periods show a very high degree of Alfvénicity. Moreover, in the quiet interval, we observe antiparallel magnetic and velocity field vectors (g). Instead, in the highly disturbed period (i), we can recognize that the change in sign follows the fluctuations of the magnetic field and, especially at the end of the interval, we observe a small decrease of ρ_{vb}.

Bottom row of Figure 2 shows the local intermittency measure (LIM; Farge 1992) for the total magnetic field fluctuations, $|\mathcal{W}_{\boldsymbol{B}}(\tau, t)|^2 = \sum_i |\mathcal{W}_i(\tau, t)|^2$ with $i = r, t, n$, defined as

$$I(\tau, t) = \frac{|\mathcal{W}_{\boldsymbol{B}}(\tau, t)|^2}{\langle |\mathcal{W}_{\boldsymbol{B}}(\tau, t)|^2 \rangle_t}, \quad (1)$$

where the brackets indicate a time average and $\mathcal{W}_i(\tau, t)$ are the Morlet wavelet coefficients for different timescales τ and time t (Torrence & Compo 1998)

$$\mathcal{W}_i(\tau, t) = \sum_{j=0}^{N-1} B_i(t_j) \psi^*[(t_j - t)/\tau]. \quad (2)$$

Black lines denote the local ion cyclotron timescale, while the curved ones, on each side of the plots, represent the cone of influence, where the Morlet coefficients are affected by edge effects (Torrence & Compo 1998). In all three intervals, the distribution of energy in time and scales is not uniform, with the appearance of localized energetic events covering a certain range of scales, which are easily recognized by the red color. This is an indication of the presence of coherent structures in the system that emerge at larger timescales and are connected through the scales (Lion et al. 2016; Perrone et al. 2016, 2017; Alexandrova et al. 2020). Similar features have also been reported by Greco et al. (2016) using the partial variance of increments technique.

Figure 3 shows the total power spectral density (i.e., the trace of the spectral matrix) of the magnetic field for the quiet (green), weakly disturbed (violet), and highly disturbed (orange) periods. The vertical solid line at $f = 10$ Hz indicates

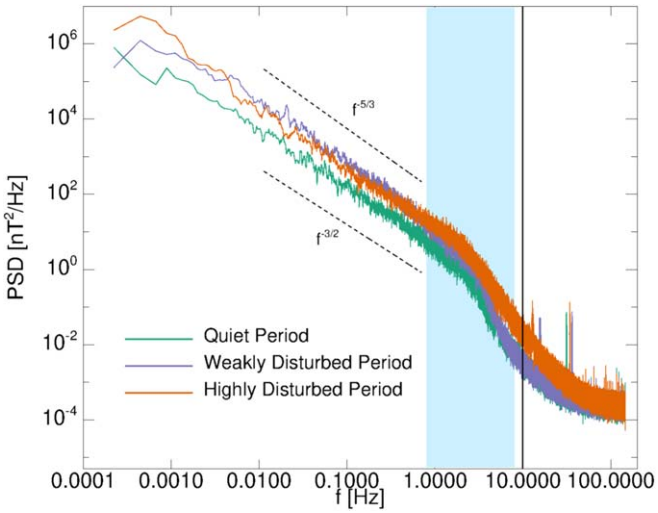

Figure 3. Power spectral density (PSD) of the total magnetic field fluctuations for the quiet (green), weakly disturbed (violet), and highly disturbed (orange) periods. Both Kolmogorov and Kraichnan scalings (black dotted lines) have been plotted for reference. The vertical black solid line indicates the maximum resolved frequency for the spectra ($f_{\max} = 10$ Hz), while the blue filled band denotes the range of scales, $f \in [0.8,8]$ Hz, around ion scales.

the frequency at which the noise level becomes significant. These spectra show the characteristic behavior of the solar wind turbulent cascade. For each stream, we observe at low frequencies a power-law trend between the Kolmogorov (Kolmogorov 1941) and the Kraichnan (Kraichnan 1965) scaling (black dotted lines). Indeed, in the inertial range, in the frequency range $f \in [0.016, 0.8]$ Hz, the spectral indices for the quiet, weakly disturbed, and highly disturbed intervals are -1.548 ± 0.015, -1.759 ± 0.014, and -1.487 ± 0.013, respectively. These values are in agreement with the results described in Chen et al. (2020) and Duan et al. (2020). However, we notice that, throughout the quiet period, although the angle θ_{BV} indicates that we are sampling the solar wind mainly parallel to the local field, the spectral index of the corresponding power density spectrum is far from the expected value of -2 predicted by the critical balance theory (GS95; Goldreich & Sridhar 1995). There are different reasons that might explain this result. The first one is that GS95 applies to strong turbulence in which opposite Alfvénic modes have the same amplitude and cross helicity is close to zero, while in our case outward modes are largely dominating. The other possibility is that the angle θ_{BV} is not small enough. To this regard, Horbury et al. (2008) showed that the spectral index for quasi-parallel sampling quickly departs from -2 for angles larger than about 10° (see also von Papen & Saur 2015), smaller than the average value we obtain in this time interval. Another possibility is that the presence of intermittency might have a steepening effect on the power spectral density and the removal of intermittency events would allow us to recover the classical $-5/3$ as shown by Wang et al. (2014). In this respect we can anticipate that the intermittent level of this time interval is rather low, as discussed later in the paper. Finally, another possibility is that GS95 does not always apply to solar wind turbulence as shown by Telloni et al. (2019). In particular, these authors remarked that in the analyzed time interval they observed a stochastic process characterized by a $-5/3$ spectral scaling, not necessarily generated by the canonical turbulence process, as indicated by the absence of intermittency, which

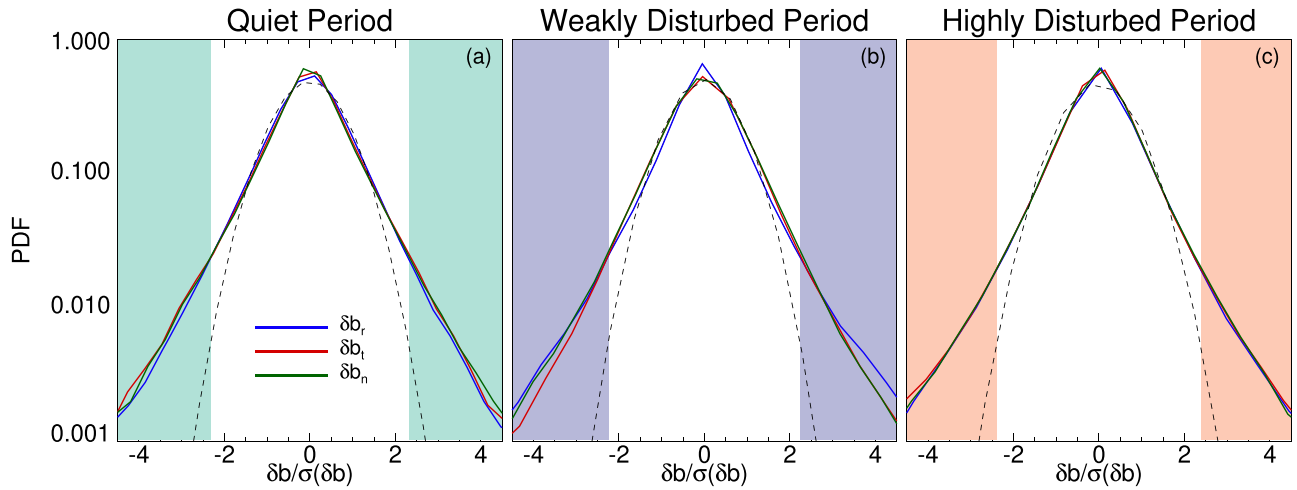

Figure 4. Probability distribution functions (PDFs) of δb_r (blue), δb_t (red), and δb_n (green), normalized to their own standard deviations, $\sigma(\delta b_i)$, for the quiet (a), weakly disturbed (b), and highly disturbed (c) periods. In each panel, black dashed lines, correspond to a Gaussian fit and the filled bands show the regions where magnetic fluctuations exceed three standard deviations of each Gaussian fit.

could be explained in the framework of the nearly incompressible model by Zank et al. (2017).

Then, a break between the inertial range and the dissipative range of the turbulent cascade can be identified around ion scales in Figure 3. The frequency location of the break for each time interval, which is around 2–3 Hz, has been estimated adopting the same procedure described in Bruno & Trenchi (2014), i.e., fitting a power law on either side of the break and finding the intersection of both curves. Although the range of frequencies between 3 and 8 Hz is not affected by noise, it is smaller than a decade in scale and is not sufficient for an accurate determination of the spectral index in the sub ion range. However, taking into account this limitation, the break appears to be closer to the prediction based on the ion cyclotron resonance mechanism (Leamon et al. 1998), in agreement with previous studies (Leamon et al. 1998; Bruno & Trenchi 2014; Woodham et al. 2018; D'Amicis et al. 2019; Duan et al. 2020). In particular, for the three different time intervals, quiet, weakly disturbed and highly disturbed, we obtain the following ion cyclotron resonance frequencies: $f_R = Vf_{ci}/(V_A + v_{th}) \simeq 2.60$ Hz, 2.53 Hz, and 2.91 Hz, respectively, considering that the ion gyrofrequency is, for the three intervals, $f_{ci} = \Omega_{ci}/(2\pi) \simeq 1.29$ Hz, 1.30 Hz, and 1.52 Hz. To compare, the timescale corresponding to both the ion Larmor radius and inertia length can be estimated, under the assumption of wavevectors parallel to the plasma flow, by using the information in Table 1. Indeed, we found $f_{\lambda_i} = V/(2\pi\lambda_i) \simeq$ 3.8 Hz, 4 Hz, 4.2 Hz, and $f_{\rho_i} = V/(2\pi\rho_i) \simeq 6.7$ Hz, 7.1 Hz, 10 Hz, for quiet, weakly disturbed and highly disturbed intervals, respectively.

For the present study we are interested in the investigation of the nature of the turbulent fluctuations around ion scales, indicated in Figure 3 by the blue filled band. Therefore, from now on, our analysis will focus on the denoted range of scales $f \in [0.8, 8]$ Hz.

3. Coherent Events

In order to look at the overall nature of the magnetic field fluctuations in the chosen range of scales, we adopt a bandpass filter based on the wavelet transform (Torrence & Compo 1998; He et al. 2012; Roberts et al. 2013; Perrone et al. 2016, 2017). The fluctuations are defined as

$$\delta b_i(t) = \frac{\delta j \delta t^{1/2}}{C_\delta \psi_0(0)} \sum_{j=j_1}^{j_2} \frac{\mathcal{R}[\mathcal{W}_i(\tau_j, t)]}{\tau_j^{1/2}}, \quad (3)$$

where $\mathcal{R}$ refers to the real-part function, j is the scale index, and δj is the constant scale step; $\psi_0(0) = \pi^{1/4}$ and $C_\delta = 0.776$, the latter derived from the reconstruction of a δ function using the Morlet wavelet (Torrence & Compo 1998). Finally, $\tau(j_1) = 0.125$ s and $\tau(j_2) = 1.25$ s (being $\tau = 1/f$).

In Figure 4, we show the probability distribution functions (PDFs) of the three components of the magnetic field fluctuations (δb_r in blue, δb_t in red, and δb_n in green), normalized to their own standard deviation, $\sigma(\delta b_i)$, for the quiet (a), weakly disturbed (b) and highly disturbed (c) intervals. By comparing the PDFs with a Gaussian fit (black dashed line), we observe the presence of significant non-Gaussian tails in each component of the magnetic field fluctuations, due to the presence of strong energetic events (Perrone et al. 2016, 2017). This result is confirmed by the flatness of the magnetic fluctuations, which has the same behavior in the three periods analyzed (not shown). We find that, in the MHD regime, the flatness monotonically increases and, at the end of the MHD range, it departs from the expected value of the flatness for a standard normal distribution (i.e., 3). Then, around the ion characteristic scales, the flatness becomes almost constant, around a value of about 5. This reflects a nonhomogeneous distribution of the turbulent fluctuations in all three periods. In each panel of Figure 4, the filled bands show the regions where magnetic fluctuations exceed three standard deviations of the Gaussian fit, which include 99.7% of the Gaussian contribution, for the compressive fluctuations (as in Perrone et al. 2016).[13] We will use the corresponding value in each period as a threshold to select non-Gaussian intermittent events. More than 1000 events have been detected in each period, thus supporting a statistical analysis of their properties.

[13] The same results, which will be described in the following part of the paper, can be found if we select intermittent events by considering a threshold on the total turbulent magnetic energy (as in Perrone et al. 2017).

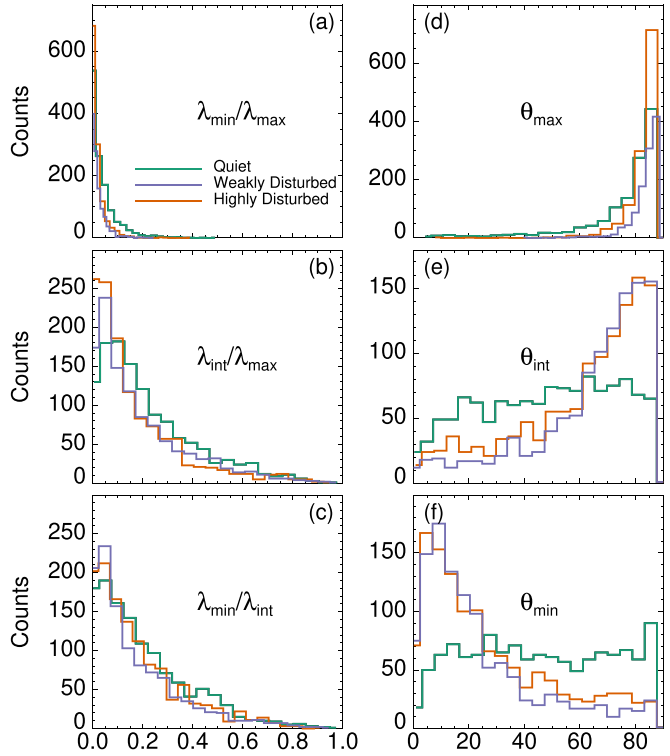

Figure 5. Statistical analysis of the observed coherent events in the minimum variance reference frame for the quiet (green), weakly disturbed (violet), and highly disturbed (orange) periods. Left panels: histograms for the minimum (a) and intermediate (b) eigenvalues normalized to the maximum eigenvalue, and for $\lambda_{min}/\lambda_{int}$ (c). Right panels: histograms of the angles between the maximum (d), intermediate (e), and minimum (f) variance directions and the local magnetic field.

3.1. Statistical Analysis

Figure 5 shows the results of the minimum variance analysis (Sonnerup & Scheible 1998) applied to the intermittent events observed in the quiet (green), weakly disturbed (violet), and highly disturbed (orange) periods. It is worth pointing out that this analysis has been performed around each selected peak in magnetic energy, which identifies magnetic fluctuations well-localized in time and with regular profiles, in a defined time range, $\Delta t'$, between two minima of energy. This corresponds to the width (i.e., extension) of an event, larger than its characteristic temporal scale, Δt, which is defined as the width at half height (see Perrone et al. 2016 for more details on the identification method for intermittent events).

The left column displays the histograms for the minimum, λ_{min} (a), and intermediate, λ_{int} (b), eigenvalues normalized to the maximum eigenvalue, λ_{max}, and for $\lambda_{min}/\lambda_{int}$ (c). Although most of the considered events, in all the intervals, have $\lambda_{min} \ll \lambda_{int} \ll \lambda_{max}$, we also find the presence of fluctuations with $\lambda_{min} \ll \lambda_{int} \lesssim \lambda_{max}$, a feature a bit more pronounced in the quiet period. In general, the minimum variance direction is well defined in all three considered periods, even if for a very few events, a degeneracy $\lambda_{min} \sim \lambda_{int}$ exists.

The right column shows the histograms of the orientation of the eigenvectors with respect to the local magnetic field, $\boldsymbol{b}_0$, also averaged within the structure, thus in $\Delta t'$. The direction of maximum variation, θ_{max} (d), is perpendicular to $\boldsymbol{b}_0$ in all three intervals, suggesting the absence of compressive events. Differences between the periods, instead, are found in the distributions of θ_{int} (e) and θ_{min} (f). In particular, we observe in the quiet period an almost uniform distribution for both θ_{int} and θ_{min}, while in the weakly disturbed and highly disturbed intervals θ_{int} is peaked around 90° and θ_{min} is almost parallel to $\boldsymbol{b}_0$. It is worth pointing out that another definition for the local magnetic field could lead to different physical results (Chen et al. 2011; Matthaeus et al. 2012; TenBarge et al. 2012). However, here, we found similar results if we consider a global magnetic field defined in each 1h15 interval. Indeed, the histogram of the angle between the global and local magnetic field (not shown) peaks at relatively small values (less than 20° for the quiet period and around 25° for both weakly and highly disturbed intervals).

To better highlight the differences between the three intervals with respect to the intermittent events observed, in Figure 6 we show the histograms of β (a), θ_{BV} (b), and $\zeta_{\parallel}$ (c), the latter being the local magnetic compressibility (Perrone et al. 2016), defined as

$$\zeta_{\parallel} = \sqrt{\frac{\max\left(\delta b_{\parallel}^2\right)}{\max\left(\delta b_{\perp 1}^2 + \delta b_{\perp 2}^2\right)}}, \tag{4}$$

where parallel and perpendicular directions are evaluated with respect to $\boldsymbol{b}_0$ and the maximum of the magnetic components is evaluated within $\Delta t'$; while β and θ_{BV} have been evaluated as mean values in the same time range. The distribution of the ion plasma beta displays three distinct peaks, which reflects the behavior of β in the whole three periods (see Table 1), i.e., the largest value is found for the events in the weakly disturbed interval and the lowest for the ones in the highly disturbed period. Three distinct peaks are also recovered for the angle between the magnetic and velocity field vectors in each event, where $\theta_{BV} \sim 20°$ for the quiet interval (green line), $30° < \theta_{BV} < 50°$ for the weakly disturbed period (violet line), and $\theta_{BV} \sim 90°$ for the highly disturbed one (orange line). This behavior suggests that the misalignment of $\boldsymbol{b}_0$ and $\boldsymbol{v}_0$ increases as the switchback activity increases. It is worth pointing out that the value of θ_{BV} gives a view of the plasma wavevectors that the spacecraft is able to measure. In particular, for $\theta_{BV} \sim 0°$ $k_{\parallel}$ are well measured, while for $\theta_{BV} \sim 90°$ $k_{\perp}$ fluctuations are observed. However, having $\theta_{BV} \sim 0°$ does not mean that $k_{\perp}$ turbulence does not exist, just that it is not measured (Bieber et al. 1996; Saur & Bieber 1999; Horbury et al. 2008).

An opposite behavior with respect to θ_{BV}, is observed, even if less marked, for the local magnetic compressibility (see Figure 6(c)). Finally, the distribution of the characteristic timescale of these events, Δt, in all three periods, is peaked at about 0.25 s (not shown), which corresponds to ∼0.3–0.4 ion cyclotron timescale or, by assuming that the frozen-in, Taylor hypothesis is fulfilled (Perri et al. 2017), to a spatial scale of ∼6–7 λ_i or ∼11–15 ρ_i.

3.2. Examples of Observed Coherent Events

A detailed analysis of all the events observed in the selected periods has allowed us to identify three different families of coherent events, all of them present in the three periods, namely (i) current sheets, (ii) vortex-like structures, and (iii) wave packets. Examples are shown in Figure 7. The top row displays the modulus of the raw magnetic field, i.e., the large-scale magnetic field as observed by PSP, where we have only taken

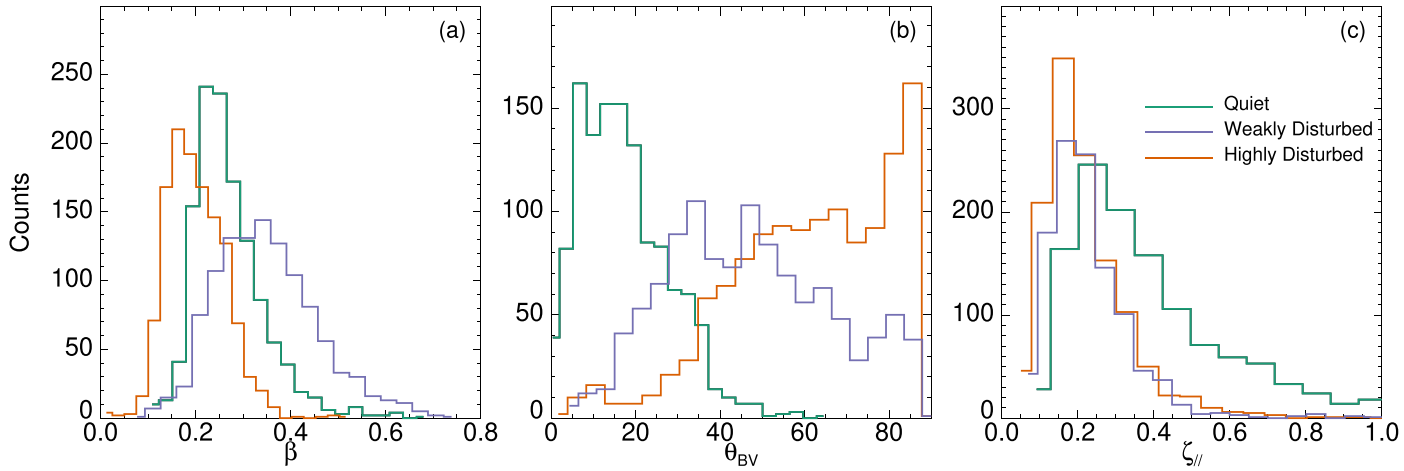

Figure 6. Histograms of β (a), θ_{BV}(b), and $\zeta_{\parallel}$ (c), for the observed coherent events in the quiet (green), weakly disturbed (violet), and highly disturbed (orange) periods.

off the noise for $f > 10$ Hz. The three panels have the same aspect ratio to highlight the magnetic compressibility of the events. Middle and bottom rows show the magnetic field fluctuations, as defined in Equation (3), in the minimum variance reference frame (MVRF) and in the local magnetic field reference frame, where $\boldsymbol{b}_0$ is along the z-direction ($\boldsymbol{e}_z = \boldsymbol{e}_b$), x is perpendicular to $\boldsymbol{b}_0$ in the plane spanned by it and the radial direction ($\boldsymbol{e}_x = \boldsymbol{e}_b \times \boldsymbol{e}_b$), and y closes the right-hand reference frame ($\boldsymbol{e}_y = \boldsymbol{e}_b \times \boldsymbol{e}_x$), respectively. Finally, vertical dashed lines mark the width of the events, $\Delta t'$, where all the analyses have been performed.

The first example of an intermittent event is a current sheet (left column), an incompressible one-dimensional (i.e., linearly polarized) structure, with δb_x (g), perpendicular to $\boldsymbol{b}_0$, which changes sign. The other two components show very small fluctuations. Moreover, the three components are almost zero in the middle of the structure, where $\delta b_{\max}$ reverses (d) and the large-scale magnetic field has a local minimum (a). Finally, the minimum variance analysis shows that the direction of maximum variation is perpendicular to $\boldsymbol{b}_0$, with $\theta_{\max} \simeq 85°$.

The second example (middle column) suggests the presence of an Alfvén vortex (Alexandrova et al. 2006; Alexandrova 2008; Lion et al. 2016; Roberts et al. 2016; Perrone et al. 2017; Wang et al. 2019). The large-scale magnetic field shows a modulated fluctuation with a local maximum in the middle of the structure (b). The fluctuations are localized, with the main variation in the direction perpendicular to $\boldsymbol{b}_0$, δb_x (h). Indeed, from the minimum variance analysis, we found that the maximum variance is perpendicular to the local magnetic field, $\theta_{\max} \simeq 87°$, while $\theta_{\rm int} \simeq 10°$ and $\theta_{\min} \simeq 80°$. In the case of a vortex, as we suppose here, where $\lambda_{\rm int} \simeq \lambda_{\min}$, the direction of minimum variance corresponds to the normal direction, while the direction of intermediate variance, which is parallel to the local magnetic field, corresponds to the vortex axis.

The last example (right column) has no clear behavior in the large-scale magnetic field (c), but δb_i show quasi-monochromatic magnetic fluctuations from -6 to 6 nT, in the plane perpendicular to $\boldsymbol{b}_0$ (i). The minimum variance analysis gives $\theta_{\max} \simeq 86°$ and $\theta_{\rm int} \simeq 85°$, while the minimum variance direction is almost parallel, $\theta_{\min} \simeq 6°$. We also note that the transverse components are out of phase of about $\pi/2$. The observed features can be associated with a wave activity.

To better highlight the polarization of these events, in Figure 8 we show the hodograms for the components of the magnetic field fluctuations in the plane perpendicular to the local magnetic field (with the local magnetic field direction out of plane) for the examples of current sheet (left), vortex-like structure (middle), and wave packet (right) shown in Figure 7. Blue star indicates the starting point, while the red square indicates the end one for the magnetic temporal signal. The first two hodograms confirm the linear polarization of both the current sheet and the vortex-like structure. Such linear polarization for vortices can be found while crossing the vortex very close to its center (see, e.g., Alexandrova & Saur 2008). On the other hand, the fluctuations of the wave packet are observed to be right-handed circularly polarized around the direction of $\boldsymbol{b}_0$. However, since the magnetic field is inward directed and assuming to have outward propagating waves, the observed wave packet is left-handed circularly polarized in the plasma frame and can be interpreted as ion cyclotron waves (He et al. 2011; Podesta & Gary 2011; Telloni et al. 2015). This is in agreement with the results in Huang et al. (2020). Ion cyclotron waves are indeed left-handed polarized waves, with a wavevector nearly aligned to the local magnetic field and frequencies around the proton gyrofrequency. In solar wind, the first observation of ion cyclotron waves was presented by Behannon (1976). They can be found in individual wave packets lasting a few minutes (Jian et al. 2009; Lion et al. 2016; Bowen et al. 2020) or in "storms" lasting many hours (Jian et al. 2010, 2014; Lion 2016; Wicks et al. 2016; Bowen et al. 2020). Their presence has also been found in numerical simulations (Pezzi et al. 2017). Ion cyclotron waves have recently been directly observed in the solar wind in periods characterized by strong Alfvénic fluctuations at inertial scales (see Telloni et al. 2019, and references therein).

4. Discussion

We have studied in detail the nature of magnetic turbulent fluctuations around the ion characteristic scales in the inner heliosphere, by using the unique opportunity offered by PSP, which is sampling the solar wind far closer than ever before. In particular, we focused on a 1 day interval around its first perihelion, at 0.17 au, where we selected three 1h15 periods characterized by a different switchback activity (looking at the

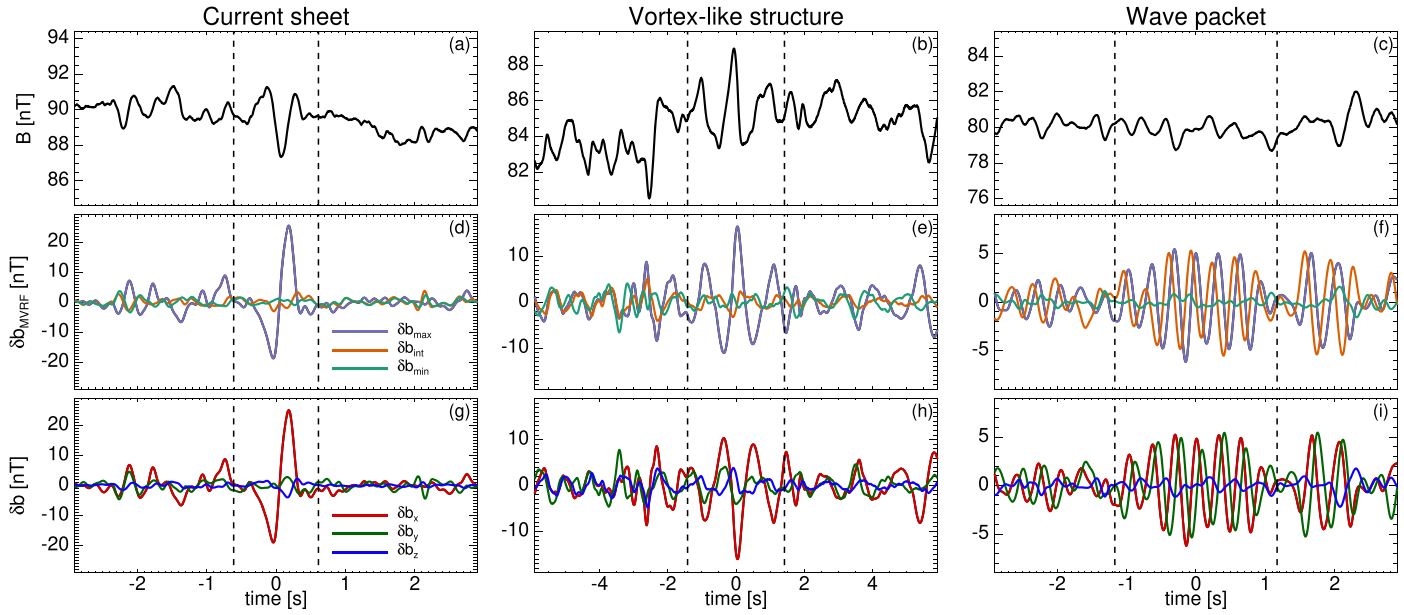

Figure 7. Example of current sheet (left column), vortex-like structure (middle column), and wave packet (right column). Top row: magnitude of the large-scale magnetic field. Middle row: components of the magnetic field fluctuations, defined in Equation (3), in the minimum variance reference frame. The maximum direction is in violet, the intermediate in orange, and the minimum in green. Bottom row: components of the magnetic field fluctuations in the local magnetic field reference frame, where $\boldsymbol{b}_0$ is along the z-direction. The vertical black dashed lines mark the extension of the events, $\Delta t'$.

behavior of B_r), and we studied magnetic properties at ion scales, thus smaller than the ones considered in Krasnoselskikh et al. (2020).

The three chosen intervals, namely quiet (B_r does not show significant fluctuations), weakly disturbed (B_r has strong fluctuations but no reversals), and highly disturbed (B_r displays full reversals), show different characteristics also in terms of large-scale plasma quantities. In particular, stronger fluctuations, in both density and temperature, are found for the whole weakly disturbed interval, while in the highly disturbed one reversals drive changes in their behavior. Moreover, we observed an increase of the presence of spikes in V_r for the weakly disturbed and highly disturbed intervals, with respect to the quiet period. Furthermore, the magnitude of both the velocity and magnetic field vectors are the same in the quiet and weakly disturbed periods, with an almost constant trend, but becomes larger, and with small changes, in the highly disturbed interval. Finally, although all three intervals show a very high level of Alfvénicity, a small decrease is observed in the highly disturbed period. It is worth pointing out that, for turbulent fluctuations at the scales considered in this work, the angle between magnetic and velocity field vectors also indicates which wavevectors are observed. Indeed, if $\theta_{BV} \sim 0°$ or $\theta_{BV} \sim 180°$, the satellite is able to scan $k_{\parallel}$, while for oblique angles $k_{\perp}$ turbulence is well measured. In this study, $k_{\parallel}$ is mostly resolved in the quiet period, while in the other two intervals θ_{BV} cover all possible angles, meaning that both $k_{\parallel}$ and $k_{\perp}$ can be measured.

The study of the spectral properties for the three considered periods showed that each stream is characterized, in the inertial range, by a power law between the Kolmogorov spectrum and the Kraichnan scaling. Then a break around the characteristic ion scales has been observed. In addition, the frequency break location seems to match the one predicted by the ion cyclotron resonance mechanism, confirming previous results based on different s/c measurements (Bruno & Trenchi 2014; Woodham et al. 2018; D'Amicis et al. 2019; Duan et al. 2020). Moreover, we also looked at the distribution of the magnetic energy in time and frequency and we found that localized regions in time that cover a certain range of scales exist in all the considered intervals. This kind of nonhomogeneity in the magnetic energy distribution has already been observed in both slow and fast wind at 1 au and it has been related to the presence, at ion scales, of different families of coherent structures or waves (Alexandrova et al. 2004; Lion et al. 2016; Perrone et al. 2016, 2017). Motivated by these results, we decided to study magnetic fluctuations in the range $f \in [0.8, 8]$ Hz, around the typical ion scales for these intervals, which are also characterized by a significant departure from Gaussianity.

We have detected more than 1000 coherent events in each period, which have well-localized fluctuations in space with regular profiles. These events can be divided into three different families, namely current sheets, vortex-like structures, and wave packets, with different influence in each considered period. A minimum variance analysis has shown that the peak of the distributions for the eigenvalues is found for $\lambda_{\rm min} \ll \lambda_{\rm int} \ll \lambda_{\rm max}$, meaning a prevalence of one-dimensional fluctuations. This is the case, for example, of the current sheets, which are the most common events in the highly disturbed period (~46% out of ~220 events for which the magnetic profile is clear), where full reversals of B_r are observed. PSP measurements have shown that the duration of the switchbacks ranges from seconds to 1 hr (Dudok de Wit et al. 2020) and that at their leading and trailing edges flowing currents are found (Krasnoselskikh et al. 2020). There, a change in the sign of the large-scale radial component of B_r is recovered, with very large amplitudes of oscillation, sometimes comparable to the magnitude of the magnetic field (Bale et al. 2019). In our analysis, for most of the current sheets we studied, no change in sign for any large-scale magnetic field component is observed. Moreover, our current sheets have characteristic timescales of about 0.5 s and amplitudes of oscillation much smaller than the one observed for the switchbacks.

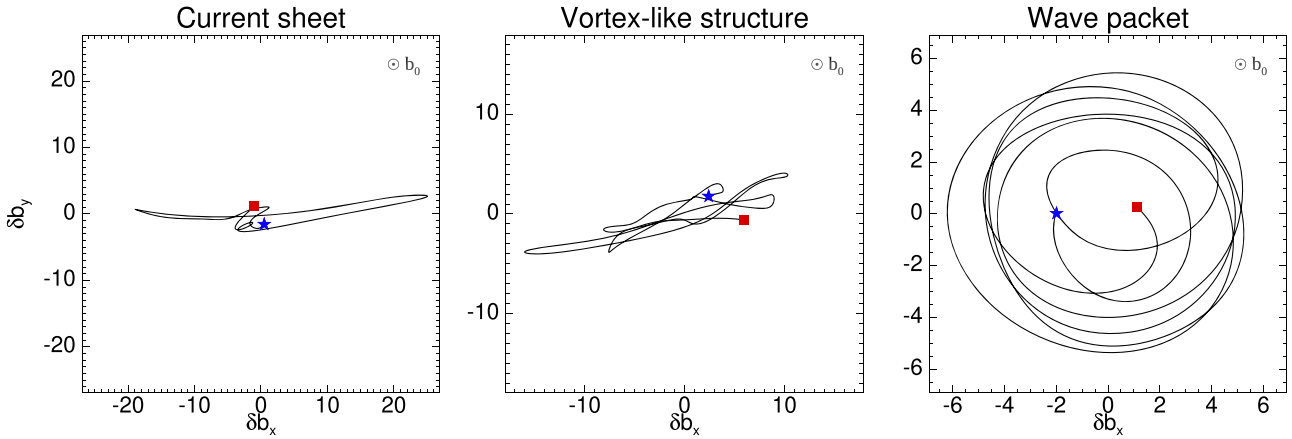

Figure 8. Hodogram for the magnetic field fluctuations of the current sheet (left), vortex-like structure (middle), and wave packet (right) shown in Figure 7, in the plane perpendicular to the local $\boldsymbol{b}_0$. Blue star refers to the starting time point and red square to the end time point.

The minimum variance analysis has also shown the presence of two-dimensional fluctuations, where $\lambda_{\rm int} \lesssim \lambda_{\rm max}$. In particular, values of $\lambda_{\rm int}/\lambda_{\rm max} \in [0.2, 0.6]$ can be recovered in the case of vortices, while $\lambda_{\rm int} \simeq \lambda_{\rm max}$ can be found for the case of wave packets. In the weakly disturbed period we observe a mixture of vortices ($\sim 45\%$ out of $\sim$342) and wave packets ($\sim$50%), while in the quiet period, where θ_{BV} is very small allowing to resolve $k_{\parallel}$ waves (Lion 2016; Bowen et al. 2020), wave packets are the most frequent class of coherent events ($\sim$61% out of $\sim$303). The left-handed circular polarization around the direction of the local magnetic field of these wave packets suggests that these wave modes can correspond to ion cyclotron waves. Evidence for the presence of ion cyclotron waves in highly Alfvénic periods supports previous findings by Telloni et al. (2019, 2020), where a clear link between the Alfvénicity at fluid scales and the existence of ion cyclotron waves at kinetic scales has statistically been proved. Moreover, ion cyclotron waves are associated with high levels of temperature anisotropy. In particular, ion cyclotron waves can lead the proton velocity distribution to depart from thermodynamic equilibrium or anisotropic proton distribution function can relax emitting waves (see e.g., Gary et al. 1994; Bourouaine et al. 2010; Telloni et al. 2019). However, in situ measurements may not be straightforward. Indeed, proton velocity distribution can become stable by the time the spacecraft observes the wave or the ion cyclotron waves can be generated by nonlocal instabilities (Podesta & Gary 2011; Klein et al. 2014; Roberts & Li 2015). Furthermore, it is also possible that ion cyclotron waves may result from a parallel cascade of fluctuations (He et al. 2011, 2012).

From the minimum variance analysis we also found that the direction of maximum variation is, in all three intervals, perpendicular to the local magnetic field, suggesting the absence of compressive events. This is in disagreement with the results in slow wind at 1 au (Perrone et al. 2016); however, the slow wind observed by PSP is highly Alfvénic, with much more similarities with the fast wind (D'Amicis et al. 2019; Perrone et al. 2020; Stansby et al. 2020; Telloni et al. 2020). In fact, we found a good agreement, for the distribution of $\theta_{\rm max}$ and $\theta_{\rm min}$ in the quiet period, with the observations in fast wind at 1 au (Perrone et al. 2017). In particular, in the quiet interval we found an almost uniform distribution for both $\theta_{\rm int}$ and $\theta_{\rm min}$, suggesting that the presence of vortices ($\sim$31%), jointly with waves (the dominant contribution), could generate a mix-up of the intermediate and minimum directions, thus all possible angles can be covered. Finally, the very low magnetic compressibility found in our analysis is also in agreement with the results in the inner heliosphere, using Helios data in the fast solar wind (Bavassano et al. 1982). It is worth pointing out that the differences between slow wind at 1 au (Perrone et al. 2016) and the one observed by PSP could also be due to the presence of stronger effect of interaction regions close to the Earth than at smaller heliocentric distances.

Understanding the role of small-scale coherent structures and waves into the general problem of dissipation, and thus heating, in collisionless plasmas, and especially in solar wind, represents a key problem for space plasma physics. In situ measurements (Marsch 2006; Bourouaine et al. 2010; Wu et al. 2013) and numerical experiments (Araneda et al. 2008; Valentini et al. 2008; Servidio et al. 2012; Perrone et al. 2013, 2014; Valentini et al. 2016) have shown that particle heating and acceleration and temperature anisotropy appear localized in and near coherent structures or due to wave-particle interactions. Unfortunately, the resolution of the particle measurements on PSP is not enough to study in detail the kinetics within the selected events (the mean width of the events is around 2 s and the resolutions for ion data is about 1 s). Preliminary results of statistical studies on the same families of structures suggest that both ion density and temperature show an increase at the edges of current sheets and vortex-like structures, and within the wave packets. Further analyses to link the presence of different families of structures to kinetic effects on particles will be the subject of our future work.

The new observations of these macroscopic magnetic switchbacks made by PSP are allowing us to add new pieces to the puzzle of the energy dissipation mechanisms in collisionless plasmas. However, the origin of such events is still unclear and under debate. Until now, several physical processes, both in situ (Ruffolo et al. 2020; Squire et al. 2020) and in the solar atmosphere (see, for instance, Tenerani et al. 2020), have been proposed to explain these switchbacks. Among the many possibilities, it was pointed out that these could be due to coronal jets and filament eruptions (Sterling & Moore 2020), to reconnection processes or to phenomena happening in the deep corona. Indeed, it has been shown, through state-of-the-art numerical modeling (Tenerani et al. 2020), that these perturbations may originate in the solar

atmosphere and propagate upwards. In this regard, it is worth noting that large amplitude kink-like oscillations are nowadays detected in high resolution observations in a plethora of magnetic structures, and at all heights in the solar atmosphere, from the corona and chromospheric heights (see, for instance, Anfinogentov et al. 2013; Jafarzadeh et al. 2017, to mention a few) down to the photosphere, where they are excited by the forcing action of the granular buffeting (Stangalini et al. 2014). Due to this, their atmospheric origin seems a reasonable explanation. In the near future, thanks to the synergy between PSP, which will collect measurements far closer to the Sun, Solar Orbiter (Muller et al. 2013), which will combine both remote sensing and in situ measurements, and DKIST, the new 4 m class solar telescope, it will be possible to provide further insights in the understanding of the link between the switchbacks in the solar wind and their possible source in the solar atmosphere.

D.T. and R.D.M. were partially supported by the Italian Space Agency (ASI) under contract I/013/12/0. O.A. was supported by the French Space Agency (CNES). The authors would like to acknowledge the anonymous referee for useful comments and suggestions that greatly helped to improve the manuscript.

ORCID iDs

Denise Perrone https://orcid.org/0000-0003-1059-4853
Roberto Bruno https://orcid.org/0000-0002-2152-0115
Raffaella D'Amicis https://orcid.org/0000-0003-2647-117X
Daniele Telloni https://orcid.org/0000-0002-6710-8142
Rossana De Marco https://orcid.org/0000-0002-7426-7379
Marco Stangalini https://orcid.org/0000-0002-5365-7546
Silvia Perri https://orcid.org/0000-0002-8399-3268
Oreste Pezzi https://orcid.org/0000-0002-7638-1706
Olga Alexandrova https://orcid.org/0000-0003-3811-2991
Stuart D. Bale https://orcid.org/0000-0002-1989-3596

References

Alexandrova, O. 2008, NPGeo, 15, 95
Alexandrova, O., Chen, C. H. K., Sorriso-Valvo, L., Horbury, T. S., & Bale, S. D. 2013, SSRv, 178, 101
Alexandrova, O., Jagarlamudi, V., Rossi, C., et al. 2020, NatCo, submitted (arXiv:2004.01102)
Alexandrova, O., Mangeney, A., Maksimovic, M., et al. 2004, JGRA, 109, A05207
Alexandrova, O., Mangeney, A., Maksimovic, M., et al. 2006, JGRA, 111, A12208
Alexandrova, O., & Saur, J. 2008, GeoRL, 35, L15102
Alexandrova, O., Saur, J., Lacombe, C., et al. 2009, PhRvL, 103, 165003
Anfinogentov, S., Nisticò, G., & Nakariakov, V. M. 2013, A&A, 560, A107
Araneda, J. A., Marsch, E., & Viñas, A. F. 2008, PhRvL, 100, 125003
Badman, S. T., Bale, S. D., Martínez Oliveros, J. C., et al. 2020, ApJS, 246, 23
Bale, S. D., Badman, S. T., Bonnell, J. W., et al. 2019, Natur, 576, 237
Bale, S. D., Goetz, K., Harvey, P. R., et al. 2016, SSRv, 204, 49
Bale, S. D., Kellogg, P. J., Mozer, F. S., Horbury, T. S., & Reme, H. 2005, PhRvL, 94, 215002
Balogh, A., Forsyth, R. J., Lucek, E. A., Horbury, T. S., & Smith, E. J. 1999, GeoRL, 26, 631
Bavassano, B., Dobrowolny, M., Fanfoni, G., Mariani, F., & Ness, N. F. 1982, SoPh, 78, 373
Behannon, K. W. 1976, PhD thesis, The Catholic Univ. of America
Behannon, K. W., & Burlaga, L. F. 1981, in Solar Wind 4, ed. H. Rosenbauer (Garching: Max-Planck-Institute für Aeronomie), 374
Bieber, J. W., Wanner, W., & Matthaeus, W. H. 1996, JGR, 101, 2511
Borovsky, J. E. 2008, JGRA, 113, A08110
Borovsky, J. E. 2016, JGRA, 121, 5055
Borovsky, J. E., & Gary, S. P. 2014, JGRA, 119, 5210
Bourouaine, S., Marsch, E., & Neubauer, F. M. 2010, GeoRL, 37, L14104
Bowen, T. A., Mallet, A., Huang, J., et al. 2020, ApJS, 246, 66
Bruno, R. 2019, E&SS, 6, 656
Bruno, R., & Carbone, V. 2013, LRSP, 10, 2
Bruno, R., Carbone, V., Sorriso-Valvo, L., & Bavassano, B. 2003, JGR, 108, 1130
Bruno, R., & Trenchi, L. 2014, ApJL, 787, L24
Carbone, F., Sorriso-Valvo, L., Alberti, T., et al. 2018, ApJ, 859, 27
Case, A. C., Kasper, J. C., Stevens, M. L., et al. 2020, ApJS, 246, 43
Chen, C. H. K., Bale, S. D., Bonnell, J. W., et al. 2020, ApJS, 246, 53
Chen, C. H. K., Mallet, A., Yousef, T. A., Schekochihin, A. A., & Horbury, T. S. 2011, MNRAS, 415, 3219
Chen, C. H. K., Sorriso-Valvo, L., Šafránková, J., & Němeček, Z. 2014, ApJL, 789, L8
Coleman, P. J., Jr 1968, ApJ, 153, 371
D'Amicis, R., & Bruno, R. 2015, ApJ, 805, 84
D'Amicis, R., Matteini, L., & Bruno, R. 2019, MNRAS, 483, 4665
Duan, D., Browen, T. A., Chen, C. H. K., et al. 2020, ApJS, 246, 55
Dudok de Wit, T., Krasnoselskikh, V. V., Bale, S. D., et al. 2020, ApJS, 246, 39
Farge, M. 1992, AnRFM, 24, 395
Fox, N. J., Velli, M., Bale, S. D., et al. 2016, SSRv, 204, 7
Freeman, J. W. 1988, GeoRL, 15, 88
Gary, S. P., Bandyopadhyay, R., Qudsi, R. A., et al. 2020, ApJ, 901, 160
Gary, S. P., McKean, M. E., Winske, D., et al. 1994, JGR, 99, 5903
Goldreich, P., & Sridhar, S. 1995, ApJ, 438, 763
Greco, A., Matthaeus, W. H., D'Amicis, R., Servidio, S., & Dmitruk, P. 2012a, ApJ, 749, 105
Greco, A., & Perri, S. 2014, ApJ, 784, 163
Greco, A., Perri, S., Servidio, S., Yordanova, E., & Veltri, P. 2016, ApJL, 823, L39
Greco, A., Valentini, F., Matthaeus, W. H., Servidio, S., & Dmitruk, P. 2012b, PhRvE, 86, 066405
He, J., Marsch, E., Tu, C., Yao, S., & Tian, H. 2011, ApJ, 731, 85
He, J., Tu, C., Marsch, E., & Yao, S. 2012, ApJL, 745, L8
Hellinger, P., Matteini, L., Landi, S., et al. 2019, ApJ, 883, 178
Hellinger, P., Trávníček, P. M., Stverák, S., Matteini, L., & Velli, M. 2013, JGRA, 118, 1351
Horbury, T. S., Forman, M., & Oughton, S. 2008, PhRvL, 101, 175005
Horbury, T. S., Woolley, T., Laker, R., et al. 2020, ApJS, 246, 45
Huang, S. Y., Zhang, J., Sahraoui, F., et al. 2020, ApJL, 897, L3
Jafarzadeh, S., Solanki, S. K., Stangalini, M., et al. 2017, ApJS, 229, 10
Jian, L. K., Russell, C. T., Luhmann, J. G., et al. 2009, ApJL, 701, L105
Jian, L. K., Russell, C. T., Luhmann, J. G., et al. 2010, JGR, 115, A12115
Jian, L. K., Wei, H. Y., Russell, C. T., et al. 2014, ApJ, 786, 123
Kahler, S. W., Crocker, N. U., & Gosling, J. T. 1996, JGR, 101, 24373
Kasper, J. C., Abiad, R., Austin, G., et al. 2016, SSRv, 204, 131
Kasper, J. C., Bale, S. D., Belcher, J. W., et al. 2019, Natur, 576, 228
Kasper, J. C., Lazarus, A. J., & Gary, S. P. 2008, PhRvL, 101, 261103
Kiyani, K. H., Chapman, S. C., Khotyaintsev, Yu. V., Dunlop, M. W., & Sahraoui, F. 2009, PhRvL, 103, 075006
Kiyani, K. H., Chapman, S. C., Sahraoui, F., et al. 2013, ApJ, 763, 10
Klein, K. G., Alterman, B. L., Stevens, M. L., Vech, D., & Kasper, J. C. 2018, PhRvL, 120, 205102
Klein, K. G., Howes, G. G., TenBarge, J. M., & Podesta, J. J. 2014, ApJ, 785, 138
Kolmogorov, A. 1941, DoSSR, 30, 301
Kraichnan, R. H. 1965, PhFl, 8, 1385
Krasnoselskikh, V., Larosa, A., Agapitov, O., et al. 2020, ApJ, 893, 93
Landi, S., Hellinger, P., & Velli, M. 2006, GeoRL, 33, L14101
Leamon, R. J., Matthaeus, W. H., Smith, C. W., & Wong, H. K. 1998, ApJL, 507, L181
Lion, S. 2016, PhD Thesis, Université Pierre et Marie Curie
Lion, S., Alexandrova, O., & Zaslavsky, A. 2016, ApJ, 824, 47
Lopez, R. E., & Freeman, J. W. 1986, JGR, 91, 1701
Marsch, E. 2006, LRSP, 3, 1
Marsch, E., Muhlhauser, K.-H., Schwenn, R., Rosenbauer, H., Pilipp, W., & Neubauer, F. M. 1982, JGR, 87, 52
Matteini, L., Landi, S., Velli, M., & Hellinger, P. 2010, JGRA, 115, A09106
Matthaeus, W. H., Oughton, S., Osman, K. T., et al. 2014, ApJ, 790, 155
Matthaeus, W. H., Servidio, S., Dmitruk, P., et al. 2012, ApJ, 750, 103

Matthaeus, W. H., Yang, Y., Wan, M., et al. 2020, ApJ, 891, 101
Muller, D., Marsden, R. G., St., Cyr, O. C., et al. 2013, SoPh, 283, 25
Osman, K. T., Matthaeus, W. H., Greco, A., & Servidio, S. 2011, ApJL, 727, L11
Perri, S., Carbone, V., Vecchio, A., et al. 2012, PhRvL, 109, 245004
Perri, S., Servidio, S., Vaivads, A., & Valentini, F. 2017, ApJS, 231, 4
Perrone, D., Alexandrova, O., Mangeney, A., et al. 2016, ApJ, 826, 196
Perrone, D., Alexandrova, O., Roberts, O. W., et al. 2017, ApJ, 849, 49
Perrone, D., D'Amicis, R., De Marco, R., et al. 2020, A&A, 633, A166
Perrone, D., Stansby, D., Horbury, T. S., & Matteini, L. 2019a, MNRAS, 483, 3730
Perrone, D., Stansby, D., Horbury, T. S., & Matteini, L. 2019b, MNRAS, 488, 2380
Perrone, D., Valentini, F., Servidio, S., Dalena, S., & Veltri, P. 2013, ApJ, 762, 99
Perrone, D., Valentini, F., Servidio, S., Dalena, S., & Veltri, P. 2014, EPJD, 68, 209
Pezzi, O., Malara, F., Servidio, S., et al. 2017, PhRvE, 96, 023201
Pezzi, O., Perrone, D., Servidio, S., et al. 2019, ApJ, 887, 208
Pezzi, O., Servidio, S., Perrone, D., et al. 2018, PhPl, 25, 060704
Podesta, J. J., & Gary, S. P. 2011, ApJ, 734, 15
Qudsi, R. A., Bandyopadhyay, R., Maruca, B. A., et al. 2020, ApJ, 895, 83
Retinò, A., Sundkvist, D., Vaivads, A., et al. 2007, NatPh, 3, 236
Roberts, O. W., & Li, X. 2015, ApJ, 802, 1
Roberts, O. W., Li, X., Alexandrova, O., & Li, B. 2016, JGRA, 121, 3870
Roberts, O. W., Li, X., & Li, B. 2013, ApJ, 769, 58
Ruffolo, D., Matthaeus, W. H., Chhiber, R., et al. 2020, ApJ, 902, 94
Sahraoui, F., Goldstein, M. L., Belmont, G., Canu, P., & Rezeau, L. 2010, PhRvL, 105, 131101
Salem, C., Hubert, D., Lacombe, C., et al. 2003, ApJ, 585, 1147
Salem, C., Mangeney, A., Bale, S. D., & Veltri, P. 2009, ApJ, 702, 537
Saur, J., & Bieber, J. 1999, JGR, 104, 9975
Servidio, S., Chasapis, A., Matthaeus, W. H., et al. 2017, PhRvL, 119, 205101
Servidio, S., Valentini, F., Califano, F., & Veltri, P. 2012, PhRvL, 108, 045001
Servidio, S., Valentini, F., Perrone, D., et al. 2015, JPlPh, 81, 325810107
Sonnerup, B., & Scheible, M. 1998, Analysis Methods for Multi-Spacecraft Data (The Netherlands: ESA)
Sorriso-Valvo, L., Catapano, F., Retinò, A., et al. 2019, PhRvL, 122, 035102
Sorriso-Valvo, L., Perrone, D., Pezzi, O., et al. 2018, JPlPh, 84, 725840201
Squire, J., Chandran, B. D. G., & Meyrand, R. 2020, ApJL, 891, L2
Stangalini, M., Consolini, G., Berrilli, F., De Michelis, P., & Tozzi, R. 2014, A&A, 569, A102
Stansby, D., Matteini, L., Horbury, T. S., et al. 2020, MNRAS, 492, 39
Sterling, A. C., & Moore, R. L. 2020, ApJL, 896, L18
Telloni, D., Bruno, R., & Trenchi, L. 2015, ApJ, 805, 46
Telloni, D., Carbone, F., Bruno, R., et al. 2019, ApJL, 885, L5
Telloni, D., D'Amicis, R., Bruno, R., et al. 2020, ApJ, 897, 167
TenBarge, J. M., Podesta, J. J., Klein, K. G., & Howes, G. G. 2012, ApJ, 753, 107
Tenerani, A., Velli, M., Matteini, L., et al. 2020, ApJS, 246, 32
Torrence, C., & Compo, G. P. 1998, BAMS, 79, 61
Tsurutani, B. T., Ho, C. M., Smith, E. J., et al. 1994, GeoRL, 21, 2267
Tu, C.-Y., & Marsch, E. 1995, SSRv, 73, 1
Valentini, F., Perrone, D., Stabile, S., et al. 2016, NJPh, 18, 125001
Valentini, F., Veltri, P., Califano, F., & Mangeney, A. 2008, PhRvL, 101, 025006
Veltri, P., & Mangeney, A. 1999, in AIP Conf. Proc. 471, Solar Wind IX, ed. S. Habble (Melville, NY: AIP), 543
von Papen, M., & Saur, J. 2015, ApJ, 806, 116
Wang, T., Alexandrova, O., Perrone, D., et al. 2019, ApJL, 871, L22
Wang, X., Tu, C., He, J., Marsch, E., & Wang, L. 2014, ApJL, 783, L9
Wicks, R. T., Alexander, R. L., Stevens, M., et al. 2016, ApJ, 819, 6
Williams, L. L., Zank, G. P., & Matthaeus, W. H. 1995, JGR, 100, 17059
Woodham, L. D., Wicks, R. T., Verscharen, D., & Owen, C. J. 2018, ApJ, 856, 49
Wu, P., Perri, S., Osman, K., et al. 2013, ApJL, 763, L30
Yordanova, E., Perri, S., Sorriso-Valvo, L., & Carbone, V. 2015, EL, 110, 19001
Zank, G. P., Adhikari, L., Hunana, P., et al. 2017, ApJ, 835, 147